Available online at www.sciencedirect.com
SCIENCE DIRECT®
International Journal of Heat and Mass Transfer 49 (2006) 984–994
International Journal of HEAT and MASS TRANSFER
www.elsevier.com/locate/ijhmt

A numerical study on the forced convection heat transfer from an isothermal and isoflux sphere in the steady symmetric flow regime

S.D. Dhole [a], R.P. Chhabra [a,*], V. Eswaran [b]

[a] Department of Chemical Engineering, Indian Institute of Technology, Kanpur 208 016, India
[b] Department of Mechanical Engineering, Indian Institute of Technology, Kanpur 208 016, India

Received 15 April 2005; received in revised form 29 August 2005
Available online 11 November 2005

Abstract

The effects of Reynolds and Prandtl numbers on the heat transfer characteristics of an unconfined sphere for different thermal boundary conditions (isothermal and isoflux) on the sphere surface have been investigated numerically by using a finite volume method for the range of conditions as $5 \leqslant Re \leqslant 200$ and $0.7 \leqslant Pr \leqslant 400$ (the maximum value of Peclet number being 2000). Based on the numerical results obtained herein, heat transfer correlations are developed for the constant temperature and the constant heat flux boundary conditions on the solid sphere surface in the steady symmetric flow regime. The variation of local Nusselt number on the sphere surface shows the effect of Prandtl number on heat transfer from a sphere in this flow regime. In addition, this work also demonstrates an approach to solve such flow problems using the Cartesian form of the field equations.

Keywords: Reynolds number; Prandtl number; Nusselt number; Sphere; Steady symmetric flow

1. Introduction

Owing to its many practical applications and scientific interest, the problem of convective heat transfer from a sphere has been studied extensively. The extensive literature on this subject has been summarized, amongst others, by Clift et al. [1], and by Polyanin et al. [2]. Analytical and experimental results in the form of correlations abound in heat transfer and transport phenomena textbooks, e.g. [3]. A cursory inspection of the available literature reveals the preponderance of studies involving the flow of air, i.e., the Prandtl number value of 0.7, e.g., see [1,2,4]. In contrast much less is known about the effect of Prandtl number on heat transfer. Based on experimental heat transfer data with water, oil and air, Whitaker [5] gave a correlation for the average Nusselt number for a sphere in an uniform free-stream for the range of Reynolds numbers as $1 \leqslant Re \leqslant 10^5$. Acrivos and Taylor [6] used the Stokesian velocity distribution to derive their well-known solution for the steady state for small values of Peclet numbers which works well for very small Reynolds numbers ($Re \ll 1$). Choudhoury and Drake [7] developed an analytical solution for unsteady heat transfer from a sphere at low Reynolds numbers ($Re < 1$) using the steady state velocity field obtained by Proudman and Pearson [8]. Dennis et al. [9] numerically studied the heat transfer from an isothermal sphere for the range of Reynolds numbers up to 20 and Prandtl numbers of O(1). Abramzon and Elata [10] carried out a numerical study for the transient heat transfer from a rigid sphere over a wide range of Peclet numbers using the Stokesian velocity distribution ($Re \ll 1$). Using the boundary layer flow approach, Ahmed and Yovanovich [11] provided an approximate analytical solution for the forced convection heat transfer from isothermal

* Corresponding author. Tel.: +91 512 2597393; fax: +91 512 2590104.
E-mail address: chhabra@iitk.ac.in (R.P. Chhabra).

0017-9310/$ - see front matter © 2005 Elsevier Ltd. All rights reserved.
doi:10.1016/j.ijheatmasstransfer.2005.09.010

Nomenclature

C_D total drag coefficient (–) [$= 2F_D/(\rho U_\infty^2 \pi R_s^2)$]
C_{Df} friction or viscous drag coefficient (–) [Eq. (7)]
C_{Dp} pressure drag coefficient (–) [Eq. (7)]
C_p specific heat of the fluid (J/kg K)
CWT constant wall temperature
D diameter of sphere (m)
F_D drag force exerted on the sphere (N)
F_s factor of safety (–) [Eq. (10)]
GCI grid convergence index
h local convective heat transfer coefficient (W/m^2K)
$\bar{h}$ average convective heat transfer coefficient (W/m^2K)
k thermal conductivity of the fluid (W/m K)
L_u upstream length from the inlet to the center of sphere (–)
L_d downstream length from the center of sphere to the outlet (–)
L_r recirculation length measured from the rear stagnation point (–)
L_x length of the computational domain (–) [$=L_u + L_d$]
L_y height of the computational domain (–)
N number of grid points [$=N_i \times N_j$]
N_i number of grid points on half sphere
N_j number of grid points on upstream/downstream symmetry line
n_s direction normal to the sphere surface (–)
Nu average Nusselt number of the sphere (–) [$= \bar{h}D/k$]
Nu_θ local Nusselt number of the sphere (–) [$=hD/k$]
p non-dimensional pressure (–) [$= p'/(\rho U_{max}^2)$]
p_∞ non-dimensional pressure at the exit (–)
Pe Peclet number (–) [$=Re \times Pr$]
Pr Prandtl number (–) [$=\mu c_p/k$]
Q numerical solution (–) [Eq. (10)]
Q_c numerical solution on a coarse grid (–) [Eq. (10)]
Q_f numerical solution on a fine grid (–) [Eq. (10)]
q_w heat flux at the surface of the sphere (W/m^2)
r_g ratio of the refinement between fine and coarse grids
Re Reynolds number (–) [$=DU_\infty\rho/\mu$]
t time (–) [$=t'/(D/U_{max})$]
T temperature (–) [$=(T' - T_\infty)/(T_w - T_\infty)$ or $(T' - T_\infty)/(q_w D/k)$]
T_∞ temperature of the fluid at the inlet (K)
T_w constant wall temperature at the surface of the sphere (K)
U_c average streamwise velocity (–)
U_∞ uniform velocity of the fluid at the inlet (m/s)
UHF uniform heat flux
UP + CD first-order upwind + central difference convective scheme
V_x component of the velocity in x-direction (–) [$= V'_x/U_\infty$]
V_y component of the velocity in y-direction (–) [$= V'_y/U_\infty$]
V_{y1} component of the velocity in y-direction for sector 1 in Fig. 3 (–) [$= V'_{y1}/U_\infty$]
V_{y2} component of the velocity in y-direction for sector 2 in Fig. 3 (–) [$= V'_{y2}/U_\infty$]
V_{y1}^n normal component of V_y velocity for sector 1 in Fig. 3 (–)
V_{y1}^t tangential component of V_y velocity for sector 1 in Fig. 3 (–)
V_{y2}^n normal component of V_y velocity for sector 2 in Fig. 3 (–)
V_{y2}^t tangential component of V_y velocity for sector 2 in Fig. 3 (–)
V_z component of the velocity in z-direction (–) [$= V'_z/U_\infty$]
V_{z1} component of the velocity in z-direction for sector 1 in Fig. 3 (–) [$= V'_{z1}/U_\infty$]
V_{z2} component of the velocity in z-direction for sector 2 in Fig. 3 (–) [$= V'_{z2}/U_\infty$]
x streamwise coordinate (–) [$=x'/D$]
y transverse coordinate (–) [$=y'/D$]
z azimuthal coordinate (–) [$=z'/D$]

Greek symbols
μ dynamic viscosity of the fluid, Pa s
ϕ dependent variable in convective boundary condition (–)
ϕ_z azimuthal angle (degree)
θ streamwise angle (degree)
θ_s angle of separation measured from front stagnation point (degree)
ρ density of the fluid (kg/m^3)

Superscripts
a overall order of the accuracy of the scheme [Eq. (10)]
$'$ dimensional variable

spheres for all Prandtl numbers and for $Re \leqslant 2 \times 10^5$. Kendoush [12] obtained an analytical solution to the forced convection heat and mass transfer across a laminar incompressible boundary layer, over the surface of a stationary isothermal sphere. Kendoush's [12] solution is valid for $Pr < 1$ (for gases) and for laminar flow with $Re > O(10^2)$.

Feng and Michaelides [13] also derived an analytical expression for the heat transfer from a sphere at low Peclet

numbers assuming the Stokesian velocity distribution. Subsequently, they [14] extended the range of these results by numerically solving the complete Navier–Stokes and thermal energy equations up to Reynolds numbers of 4000 and $Pr \leqslant 1000$. It is perhaps appropriate to add here that despite the fact that the flow around a sphere becomes asymmetric and time dependent for $Re > 200$, but the time averaged values of drag coefficient and Nusselt number do not seem to differ significantly from the values based on the steady state assumption [15,16].

All the aforementioned numerical studies are based on the use of the constant wall temperature boundary condition at the surface of the sphere, and all except Feng and Michaelides [14], are concerned with either low $Re(\ll 1)$ and/or low $Pr(<1)$. While the values of Prandtl number up to 50–100 are frequently encountered in chemical, petroleum and oil industries, no detailed study is available elucidating the effect of Prandtl number on the local Nusselt number behavior and the effect of different thermal boundary conditions for moderate Reynolds number flows. Owing to the generally high viscosity of such process streams, the Reynolds numbers often are not excessively high and therefore the assumptions of steady and axisymmetric flow are justified under these conditions.

The main objective of the present work is to study the role of Prandtl number and of different thermal boundary conditions on the heat transfer characteristics of a sphere in the Reynolds number range of steady axisymmetric regime. The numerical results have been used to develop simple expressions for the prediction of mean heat transfer coefficient for a sphere over the range of Prandtl numbers as $0.7 \leqslant Pr \leqslant 400$ and Reynolds numbers as $5 \leqslant Re \leqslant 200$, subject to the maximum Peclet number of 2000. Furthermore, included here is also the local Nusselt number variation along the sphere surface for both boundary conditions, which has not been presented in detail by any of the previous studies, e.g. [1,14]. Also, this work presents a new approach to the modeling of a flow past a sphere problem, which uses the Navier–Stokes equations in the Cartesian coordinate system. This approach can readily be extended to solve the 3-D and unsteady flow conditions past a sphere encountered at $Re > 200$.

2. Problem statement and mathematical formulation

The 2-D flow of an incompressible fluid with an uniform velocity U_∞ and temperature T_∞ over a sphere of diameter D placed in an infinite medium is simulated by considering the flow in a tubular domain with a sphere placed symmetrically on the tube axis with slip boundary conditions prescribed on the tube walls (Fig. 1). The length and diameter of the tubular domain are L_x and L_y. The sphere is situated at an upstream distance of L_u from the inlet of the tube to the center of the sphere and at a downstream distance of L_d from the center of the sphere to the outlet of the tube. The surface of the sphere is taken to be either at a constant temperature, T_w (CWT) or at a uniform heat flux, q_w (UHF).

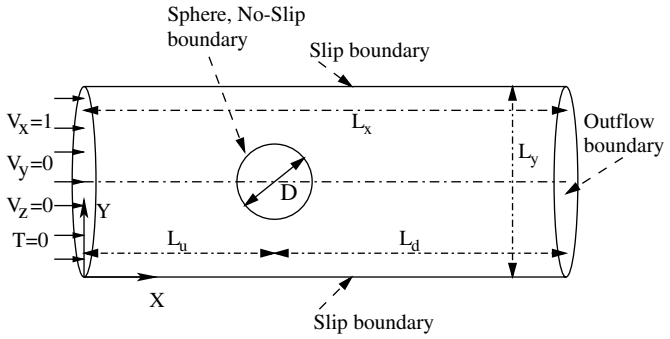

Fig. 1. Schematics of the flow past a sphere.

While in practice, the thermal boundary conditions on the surface of the sphere can be complex and ill-defined, but the two commonly used conditions of isothermal sphere or isoflux sphere capture the limiting cases. The latter condition is encountered in situations when a sphere wound with an electric coil is used as a measuring probe or sensor. Incompressible flow, constant thermo-physical properties of the fluids and negligible viscous dissipation are assumed in this work.

The governing equations are made dimensionless by using D, U_∞, D/U_∞ and ρU_∞^2 as scaling variables for lengths, velocities, time and pressure, respectively. The temperature is non-dimensionalized by using $(T_\mathrm{w} - T_\infty)$ or $(q_\mathrm{w} D/k)$ as the characteristic temperature difference for CWT and UHF conditions, respectively. All equations and numerical values presented hereafter in this work are in dimensionless form.

The flow and heat transfer phenomena is governed by the continuity, the Navier–Stokes and the energy equations as given below. The 3-D form of the governing equations in the Cartesian coordinates is maintained since the source code [17,18] in FORTRAN used in the present work is designed to solve 3-D flows past complex geometries, using Cartesian velocity components and a structured collocated grid.

Continuity equation:

$$\nabla \cdot U = 0 \tag{1}$$

Navier–Stokes equation:

$$\frac{\mathrm{D}U}{\mathrm{D}t} = -\nabla p + \frac{1}{Re}\nabla^2 U \quad \text{where } U = (V_x, V_y, V_z) \tag{2}$$

Energy equation:

$$\frac{\mathrm{D}T}{\mathrm{D}t} = \frac{1}{Pe}\nabla^2 T \tag{3}$$

The dimensionless boundary conditions are given as follows:

- *At the inlet boundary*: Uniform flow condition

$$V_x = 1; \quad V_y = 0; \quad V_z = 0; \quad \frac{\partial p}{\partial x} = 0 \quad \text{and} \quad T = 0$$

- *At the upper boundary (pipe wall)*: Slip flow condition

$$\frac{\partial V_x}{\partial y} = 0; \quad V_y = 0; \quad V_z = 0;$$

$$\frac{\partial p}{\partial y} = 0 \quad \text{and} \quad \frac{\partial T}{\partial y} = 0 \text{ (adiabatic)}$$

- *On the sphere surface*: No-slip condition

$$V_x = V_y = V_z = 0; \quad \frac{\partial p}{\partial n_s} = 0 \quad \text{and}$$

$$T = 1 \text{ (CWT case)} \quad \text{or} \quad \frac{\partial T}{\partial n_s} = -1 \text{ (UHF case)}$$

where n_s represents the unit normal vector on s, the surface of sphere.

- *At the exit boundary*: The Orlanski [19] boundary condition has been used at the exit boundary for all dependent variables except for pressure:

$$\frac{\partial \phi}{\partial t} + U_c \frac{\partial \phi}{\partial x} = 0$$

where ϕ is any dependent variable (V_x, V_y, V_z, T) and U_c is the dimensionless average streamwise velocity which is set equal to 1. The pressure at the outlet is set to a constant i.e., $p = p_\infty = 0$.

- *At the plane of symmetry, i.e., at the axis of pipe*:

$$\frac{\partial V_x}{\partial y} = 0, \quad V_y = V_z = 0, \quad \frac{\partial p}{\partial y} = 0 \quad \text{and} \quad \frac{\partial T}{\partial y} = 0$$

- *At the spherical plane of symmetry, i.e., in the azimuthal (z) direction*: Since the range of the Reynolds numbers considered in this study is well within the 2-D symmetric flow regime, the solution is obtained only for one half of the domain in Fig. 1 and a 3-D sector consisting of three cells in the z-direction (azimuthal direction) as shown in Fig. 2(a). Only three cells are required in the azimuthal direction, as the two side cells (left cells and right cells (Fig. 3)) are present to enforce the axisymmetry boundary conditions (see Appendix A) while the central cells capture the 2-D flow structure. Fig. 2(b) shows the zoom in view of the grid near the sphere. The 2-D view of Fig. 2(a) is shown in Fig. 3.

The numerical solution of Eqs. (1)–(3) along with these boundary conditions yields the velocity, pressure and temperature fields which, in turn, are used to obtain the surface vorticity, pressure coefficient, individual and total drag coefficients, and Nusselt number, as discussed below:

- The dimensionless vorticity at the surface of the sphere is calculated as follows:

$$\omega = \frac{1}{2}\left(\frac{\partial V_x}{\partial n_s}\sin\theta + \frac{\partial V_y}{\partial n_s}\cos\theta\right) \tag{4}$$

where θ is the angular displacement from the front stagnation point, and n_s is the normal direction on the sphere surface.

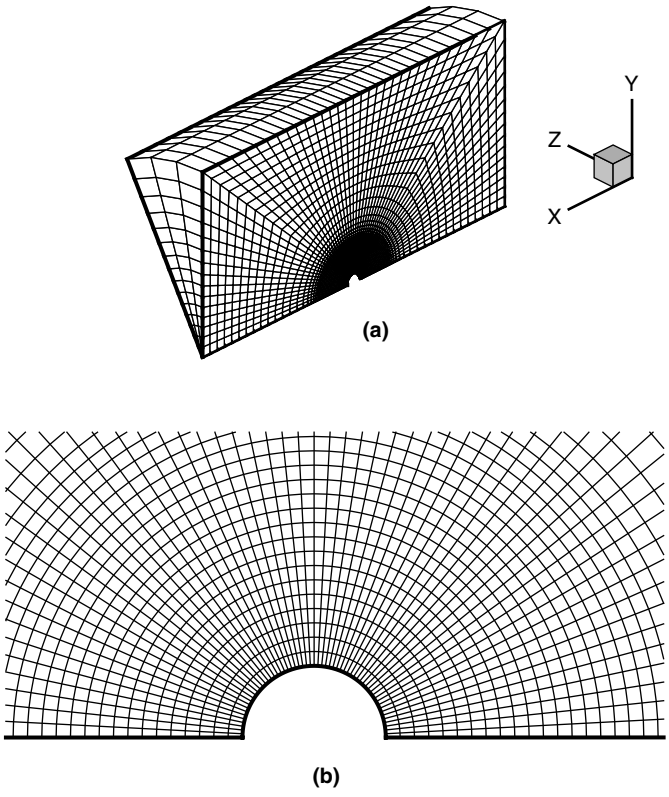

Fig. 2. Schematic representation of non-uniform computational grid structure: (a) full grid and (b) close-up view near the sphere.

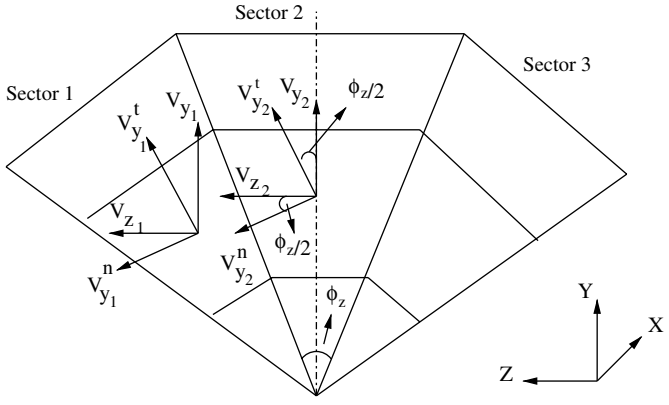

Fig. 3. 2-D view of the grid in y–z plane showing implementation of boundary conditions in z-direction.

- The pressure coefficient defined as the ratio of the static pressure to dynamic pressure on the surface of the sphere, is calculated by the following expression:

$$C_p = 2\left(\frac{p'(\theta) - p'_\infty}{\rho U_\infty^2}\right) \tag{5}$$

where $p'(\theta)$ is the surface pressure at an angular position of θ and p'_∞ is the free-stream pressure at the exit boundary.

- The total drag coefficient, sum of the viscous and the pressure drag coefficients, is defined as

$$C_D = \frac{2F_D}{\rho U_\infty^2(\pi R_s^2)} = C_{Df} + C_{Dp} \quad (6)$$

The viscous and pressure drag coefficients, C_{Df} and C_{Dp} are evaluated as follows:

$$C_{Df} = \frac{4}{Re}\int_0^\pi \omega \sin^2\theta \, d\theta \quad \text{and}$$

$$C_{Dp} = \int_0^\pi C_p \sin 2\theta \, d\theta \quad (7)$$

- The local Nusselt number on the surface of the sphere is evaluated by the following expressions:

$$Nu_\theta = -\frac{\partial T}{\partial n_s} \text{ (CWT case)} \quad \text{and} \quad Nu_\theta = \frac{1}{T} \text{ (UHF case)} \quad (8)$$

These local values have been further averaged over the whole sphere to obtain the surface average (or overall mean) Nusselt number:

$$Nu = \frac{1}{2}\int_0^\pi Nu_\theta \sin\theta \, d\theta \quad (9)$$

The average Nusselt number can be used in process engineering design calculations to estimate the rate of heat transfer from the sphere in the constant wall temperature case, or to estimate the average surface temperature of the sphere for the uniform heat flux condition in a new application.

3. Numerical methodology

3.1. Grid generation

The schematic representation of the 3-D non-uniform grid structure used in this work is shown in Fig. 2. For this type of geometry, a suitable grid may be generated by an appropriate combination of the methods of linear interpolation, hyperbolic tangent spacing interpolation and transfinite interpolation in different regions, as described in [20].

Since the sphere is placed symmetrically and the flow also exhibits axisymmetry in the range of Reynolds numbers studied here, the grid needs to be generated only in one half of the domain having three cells (middle real cell and side fictitious cells (Fig. 3)) in the third (azimuthal) direction as shown in Fig. 2. In this case, the computational domain is divided into three sub-domains and uniform and non-uniform grid distributions are applied to obtain a suitable grid. This has the advantage that grid points can be clustered in the regions of large gradients and a relatively coarse grid can be used in the regions of minor interest. The grid has been distributed uniformly along the sphere surface. Since the available literature suggests the wake region at the highest Reynolds number, i.e., $Re = 200$ used in this work can extend up to 1.5 non-dimensional units downstream, the clustered region is fixed to be within a radial distance of 2.5 from the center of the sphere, to capture the wake region. In the clustered region, a circular grid of fine and uniform spacing is generated. In the next region 2.5 units beyond the clustered region, the non-uniform grid is generated by using hyperbolic tangent spacing interpolation, to stretch the grid spacing from finer to coarser. In the next region, i.e., beyond the stretched grid region, a grid with coarser spacing is created using the transfinite interpolation.

3.2. Numerical technique

The finite volume method of Eswaran and Prakash [17] for complex 3-D geometries on a non-staggered (collocated) grid has been used to discretized and solve the governing equations with a Semi-Implicit scheme. Hence, all dependent variables V_x, V_y, V_z, p and T are defined at the centroid of the control volume. The convective terms are discretized using QUICK scheme [18,21], while the diffusive terms are discretized using the central difference scheme. The final equations were solved using a Gauss–Seidel iterative algorithm. The fully converged velocity field obtained from the Navier–Stokes equations was used as input to the thermal energy equation.

Since the cell-centered finite volume method is being used, a zero-volume cell at each boundary has been implemented to ensure that outermost cell-centers coincide with the real physical boundary. This enables the exact boundary conditions to be implemented at the surface of the sphere. The implementation of the boundary conditions with a zero-volume cell differs from that of fictitious cells of finite volume, because the cell of a zero volume coincides with the physical boundary. Thus, Dirichlet conditions can be assigned directly to these cells. The FORTRAN source code developed here has been extensively benchmarked for the lid-driven cavity flow problem using the results of Ghia et al. [22] and for the backward-facing step problem with the results of Verma and Eswaran [23].

4. Results and discussion

Numerical computations have been carried out for Reynolds numbers ranging from 5 to 200 and for various Prandtl numbers ranging from 0.7 to 200 (maximum value of Peclet number is 2000). The effect of CWT and UHF boundary conditions has been studied for the above-mentioned ranges of conditions.

4.1. Domain and grid independence

In the range of Reynolds numbers considered here, two flow regimes are known to occur, i.e., 2-D steady flow without wake formation for $Re < 20$, and 2-D steady flow with wake formation for the range $20 \leqslant Re \leqslant 200$. Therefore, the domain independence has been carried out separately for these two flow regimes. The domain is assumed with $L_u = L_d = L_y/2$. For the range $20 \leqslant Re \leqslant 200$, in the literature [14,24,25] the radial distance from the center of the

sphere to the outer boundary of the computational domain, hereafter called the domain size, varies from 30 to 90 times the radius of the sphere. Therefore, the domain independence study for this Reynolds number range has been carried out using domain sizes of 20 and 90. For $Re < 20$, in the literature [14,25] the domain size varies from 90 to 130 and hence the domain independence study has been performed for domain sizes of 100 and 130 in this flow regime. The grid size used for the domain study has a minimum spacing of $0.01D$ in the clustered region and a maximum spacing of $0.5D$ in the outer region. The number of grid points on the sphere surface was 101. The grid size used for the computations was $101 \times N_j$, where N_j varies with the size of the domain. Table 1 shows that as the domain size varies from 20 to 90, the changes in the values of C_{Dp},C_{Df} and C_D are found to be 0.88%, 0.39% and 0.57% for $Re = 20$ and 0.026%, 0.28% and 0.15% for $Re = 200$, which is <1% for these extreme values of the Reynolds number for the 2-D steady flow with wake formation regime. Therefore, the domain size of 90 is chosen to carry out the present computations, which is also consistent with the previous studies [14,25]. For $Re < 20$, the domain independence study is carried out for domain sizes of 100 and 130 at $Re = 5$. Again it can be seen from Table 1 that as the domain size changes from 100 to 130, the resulting change in the values of C_{Dp},C_{Df} and C_D is found to be 1.07%, 0.66% and 0.79%. To be on the safer side for this flow regime ($Re < 20$), the domain size of 130 is finally chosen to carry out the computations.

Having fixed domain size, the grid independence was carried out for the two flow regimes, i.e., $Re < 20$ and $20 \leqslant Re \leqslant 200$. For a domain size of 90, and the range of $20 \leqslant Re \leqslant 200$, the grid independence study was carried out by employing five non-uniform grids at $Re = 100$. Table 2 shows the effect of grid size on the drag values. The resulting maximum change in the drag values while moving from grid 103×200 to 103×307 is 0.48%. The grid meshing around the sphere for grid 5 is $0.01D$ which is fine enough to resolve the boundary layer, ($\delta = 1.13/Re^{1/2}$) [26], where δ is the momentum boundary layer thickness at the stagnation point non-dimensionalized by the diameter of the sphere. Similarly the grid independence study is shown in Table 2 for two grid sizes for the $Re < 20$ range at $Re = 5$. The grid size of 63×240 is with the meshing of $0.02D$ near sphere and the grid size of 103×298 is with the meshing of $0.01D$ near sphere. It can be seen from Table 2 that the resulting maximum change in the drag values with these two grids is 0.29% at $Re = 5$. Though the boundary layer is comparatively thick at $Re < 20$ and the grid size of 63×240 can serve the purpose, but still the fine mesh of $0.01D$ is used so that there is adequate number of grid points within the thermal boundary layer at high Peclet numbers (thermal boundary layer $\delta_t \approx Pr^{-1/3}\delta$). Therefore, grid size of 103×298 was finally chosen for the present computations. The corresponding change in the values of the Nusselt number with these domain and grid sizes is found to be less than 1% for $Re = 5$ and 100 and $Pr = 7$.

Table 1
Domain independence study

Domain size	C_{Df}	C_{Dp}	C_D
$Re = 5$			
100	4.7358	2.2355	6.9713
130	4.7671	2.2597	7.0267
$Re = 20$			
20	1.7290	0.9778	2.7068
90	1.7223	0.9693	2.6915
$Re = 200$			
20	0.3606	0.3847	0.7453
90	0.3596	0.3846	0.7442

Table 2
Grid independence study

Grid size	C_{Df}	C_{Dp}	C_D
$Re = 100$			
63×112	0.5263	0.4938	1.0201
63×135	0.5639	0.4807	1.0445
103×146	0.5700	0.4915	1.0616
103×200	0.5787	0.4846	1.0633
103×307	0.5796	0.4823	1.0619
$Re = 5$			
63×240	4.7567	2.2531	7.0098
103×298	4.7671	2.2597	7.0267

Finally, in such numerical studies, it is important to keep in mind that there is inherent uncertainty [27] in the results due to the grid size and the inaccuracy of the scheme. This point unfortunately is often ignored. However, an attempt is made to estimate this uncertainty due to the grid size and scheme accuracy used in this work. Following Roache [27], it is possible to estimate the uncertainty using the results on two different grid sizes, one fine and the other relatively coarse. According to the Grid Convergence Index (GCI) method [27], the fractional uncertainty in any quantity Q obtained through the numerical solution on the fine grid can be estimated as

$$\mathrm{GCI}(Q_f) = \left(\frac{F_s}{r_g^a - 1}\right)\left(\frac{|Q_f - Q_c|}{Q_f}\right) \tag{10}$$

where subscripts "f" and "c" stand for values computed on the fine and coarse grids, respectively, F_s is a factor of safety (assumed 3 for general applications), "a" is the overall order of the accuracy of the scheme, r_g is the ratio of the refinement between the fine and coarse grids calculated as

$$r_g = \sqrt{N_f/N_c} \tag{11}$$

where $N(= N_i \times N_j)$ is the number of grid points. The quantitative uncertainty in the value obtained on the fine grid is given as

$$\%\ \text{Uncertainty} = \pm(\mathrm{GCI} \times Q_f \times 100) \tag{12}$$

In the present work, central difference discretization is used for diffusion terms. For the convection terms, QUICK scheme has been used. Therefore, the overall method is of second-order accuracy i.e., $a = 2$. In the present study the grid uncertainty has been carried out for grids 2 and 5 i.e. (63×135) and (103×307) at $Re = 100$. For a non-uniform grid, where r_g is the ratio computed using N_c for second grid with N_f of the fifth grid. Thus, r_g from Eq. (11) becomes 1.94. Therefore, the GCI over C_D is 1.8%. A safer, more conservative estimate is obtained by using the smaller of the two directional r_g's (i.e., $r_g = 102/62 = 1.645$ along θ and $r_g = 306/134 = 2.284$ along radial direction) giving GCI = 2.88%, which is consistent with the previous studies as will be seen in the following section.

4.2. Validation

4.2.1. Drag coefficient

In order to validate the solver used in the present study, the present values of the drag coefficient for an isothermal sphere have been compared with those of Feng and Michaelides [14], Johnson and Patel [24], LeClair [25], Tripathi et al. [28], Fornberg [29], and Dennis and Walker [30].

Table 3 shows a comparison of the present results with previous results. The results are seen to be in good agreement, within overall differences of ±3% to 4%. Such deviations are not uncommon in numerical studies due to the differences in the flow schematics, problem formulations, grid and/or domain sizes, discretization schemes, numerical methods, etc. Furthermore, additional computations have been carried out by using UP + CD scheme for the convective terms and the maximum deviation is of around 2–3% with the previous studies. The difference between the present results and the previous studies using QUICK scheme is more than that for UP + CD scheme because all of the previous numerical studies are based on either first- or second-order upwinding. Even all the previous studies [14,24,25,28–30] differ with the maximum of 3–4% when compared with each other. It must be mentioned here that all of the recent studies [14,24,28] have solved the governing equations in spherical coordinates and the present formulation is based on the Cartesian coordinate system and the fact that the present results are consistent with the previous literature studies testifies to the validity of the use of Cartesian coordinate system for this geometry. In addition to the values of drag coefficients, Tables 4 and 5 present extensive comparisons between the present values of the pressure coefficient $C_p(0)$ and $C_p(\pi)$, length of recirculation region (L_r), angle of separation (θ_s) with the literature values. Once again, the present results are seen to be in good agreement with the contemporary values available in the literature. Further comparisons performed in terms

Table 4
Comparison of pressure coefficients with literature

Reference	$C_p(0)$	$-C_p(\pi)$	$C_p(0)$	$-C_p(\pi)$
	$Re = 5$		$Re = 10$	
Present work	2.411	1.162	1.773	0.604
Dennis and Walker [30]	2.599	1.203	1.878	0.654
LeClair [25]	2.601	1.163	1.869	0.606
	$Re = 20$		$Re = 50$	
Present work	1.433	0.330	1.189	0.190
Dennis and Walker [30]	1.471	0.322	–	–
LeClair [25]	1.469	0.326	–	–
	$Re = 100$		$Re = 200$	
Present work	1.098	0.155	1.055	0.111

Table 3
Comparison of drag values with literature

Reference	C_{Df}	C_{Dp}	C_D	C_{Df}	C_{Dp}	C_D
	$Re = 5$			$Re = 10$		
Present work	4.7671	2.2597	7.0267	2.8113	1.470	4.2813
Feng and Michaelides [14]	4.694	2.346	7.040	–	–	–
Tripathi et al. [28]	–	–	–	2.785	1.5254	4.3104
Dennis and Walker [30]	4.738	2.472	7.210	2.854	1.570	4.424
LeClair [25]	4.677	2.444	7.121	2.801	1.536	4.337
	$Re = 20$			$Re = 50$		
Present work	1.7223	0.9693	2.6915	0.9233	0.6286	1.5519
Feng and Michaelides [14]	1.694	0.988	2.682	–	–	–
Johnson and Patel [24]	–	–	–	–	–	1.569
Tripathi et al. [28]	–	–	–	0.8987	0.6509	1.5496
Dennis and Walker [30]	1.708	1.024	2.730	–	–	–
LeClair [25]	1.719	1.017	2.736	–	–	–
	$Re = 100$			$Re = 200$		
Present work	0.5796	0.4823	1.0619	0.3596	0.3846	0.7442
Feng and Michaelides [14]	0.5714	0.5234	1.0948	–	–	–
Johnson and Patel [24]	–	–	1.094	–	–	0.771
Tripathi et al. [28]	0.543	0.4763	1.0192	0.3466	0.3065	0.6531
Fornberg [29]	0.5765	0.5087	1.0852	0.3590	0.4093	0.7683
LeClair [25]	0.590	0.507	1.096	0.372	0.400	0.772

Table 5
Comparison of recirculation length and angle of separation with literature

Reference	$Re = 50$		$Re = 100$		$Re = 200$	
	L_r	θ_s	L_r	θ_s	L_r	θ_s
Present work	0.41	139.68	0.88	127	1.43	116
Johnson and Patel [24]	0.404	138	0.865	126	1.439	115
Fornberg [29]	–	–	0.872	–	1.434	–
Clift et al. [1]	–	139.26	–	126.52	–	116.42
LeClair [25]	–	–	0.94	126	–	116
Taneda [31]	0.45	139	0.937	126	–	119

of the surface vorticity and surface pressure with the literature values, also showed an excellent agreement between the present and the literature values [25].

4.2.2. Nusselt number

Using the fully converged velocity field, the thermal energy equation is solved for the temperature field to obtain the local and average Nusselt numbers as functions of the Reynolds number, Prandtl number and the boundary condition. Fig. 4 shows the comparison of the present results for CWT condition at Prandtl numbers 0.7, 5 and 10 with Whitaker's [5] correlation given here as Eq. (13), which is based on experiments with air, water and oil for $1 \leqslant Re \leqslant 10^5$ and the correlation (14), proposed by Feng and Michaelides [14] which is based on their steady state numerical results for $0.1 \leqslant Re \leqslant 4000$ and $0.2 \leqslant Pe \leqslant 2000$. It needs to be emphasized here that the Whitakar's [5] correlations for flat plate, single cylinder and single sphere have gained wide acceptance, are easy to use, and are quite satisfactory for most of the design calculations and indeed are cited widely in most books, e.g. [4]. The present numerical results are well within the uncertainty

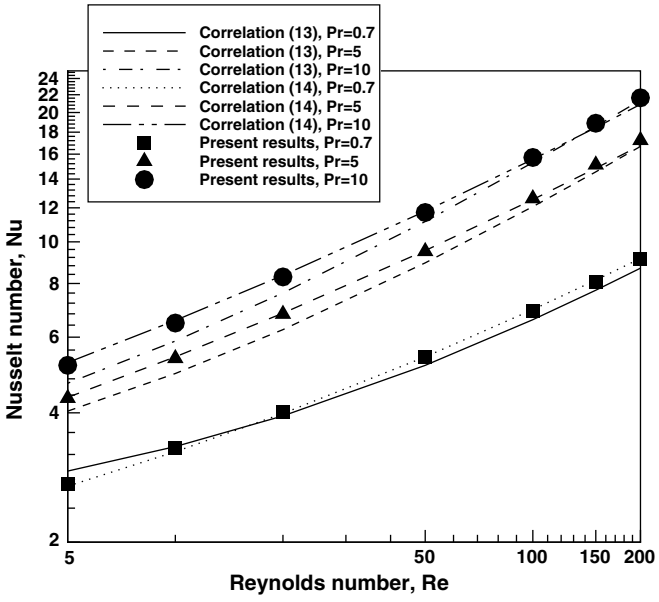

Fig. 4. Comparison of average Nusselt number with correlations.

(20%) of the Whitaker's [5] correlation, and a maximum deviation of 3% is observed from Eq. (14) of Feng and Michaelides [14].

$$Nu = 2 + (0.4Re^{1/2} + 0.06Re^{2/3})Pr^{0.4}\left(\frac{\mu}{\mu_{wall}}\right)^{1/4} \quad (13)$$

$$Nu = (0.922 + Pe^{1/3} + 0.1Re^{1/3}Pe^{1/3}) \quad (14)$$

In summary, thus the present results exhibit good correspondence with the previous experimental and numerical studies and the present results for Nusselt number may be regarded to be reliable within 2–3%. This also inspires confidence in the use of the Cartesian form of the field equations for such flow problems.

4.3. Heat transfer results

4.3.1. Local Nusselt number

Due to the inherent underlying differences, the results for the two thermal boundary conditions are discussed separately.

4.3.1.1. Constant temperature condition (isothermal sphere). The variation of the local Nusselt number on the sphere surface for the CWT condition at $Re = 5$, 50 and 200 for a range of values of the Prandtl number is shown in Fig. 5(a)–(c). As expected, the Nusselt number increases with an increase in the Reynolds number and/or Prandtl number. Fig. 5(a) shows the relatively large value of the Nusselt number at the front stagnation point ($\theta = 0°$) which decreases gradually along the surface of the sphere, to a minimum value at the rear stagnation point. For $Re > 20$, i.e., when flow separation occurs, Fig. 5(b) and (c) shows that the Nusselt number decreases from its maximum at the front stagnation point ($\theta = 0°$) to a minimum value near the point of separation, beyond which a very gradual increase in the values of local Nusselt number can be seen up to the rear stagnation point. The change in the slope in the Nusselt number variation after the separation point is evidently due to the existence of a vortex. It can also be seen that the local Nusselt number is strongly influenced by the value of the Prandtl number. At $Re = 5$, the local Nusselt number at the front stagnation point increases from 3.6 to 25.2 as the Prandtl number increases from 0.7 to 400. However, the increase in the Nusselt number at the rear stagnation point is comparatively small, i.e., from 2.04 to 2.28. On the other hand, at $Re = 200$, the front stagnation Nusselt number increases from 16.7 to 43.7 while the rear stagnation Nusselt number increases from 7.6 to 23.2 as Prandtl number increases from 0.7 to 10.

4.3.1.2. Uniform heat flux condition (isoflux sphere). Representative results on the variation of the local Nusselt number on the surface of the sphere for this case are shown in Fig. 5(d)–(f). These figures show qualitatively similar

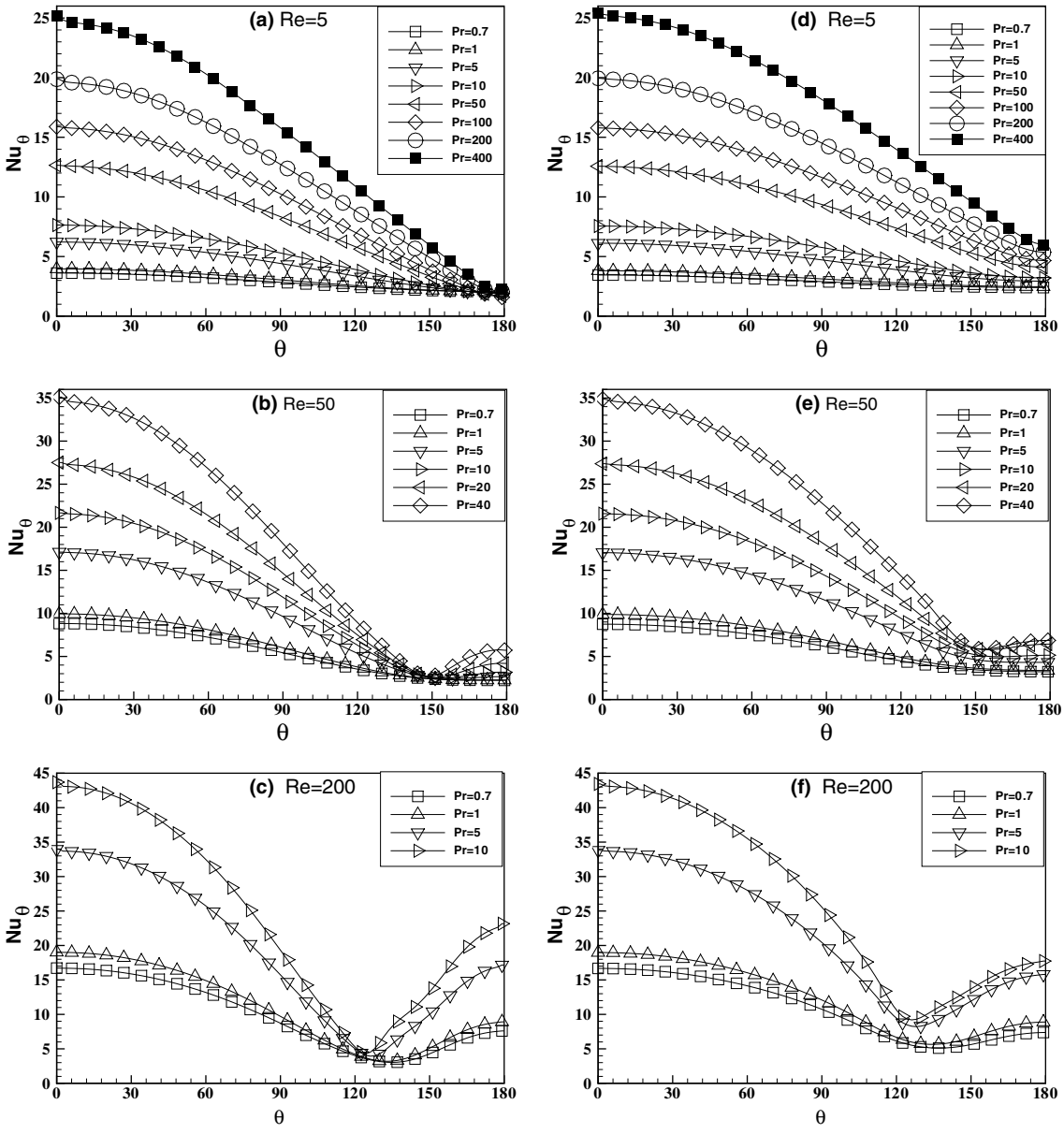

Fig. 5. Local Nusselt number variation on the sphere surface for $Re = 5$, $Re = 50$ and $Re = 200$ at various Prandtl numbers for both CWT (a–c) and UHF (d–f) conditions.

features to those in Fig. 5(a)–(c) for the CWT boundary condition.

4.3.2. Average Nusselt number

Fig. 6(a) and (b) shows the variation of the average Nusselt number with the Reynolds number at different Prandtl numbers for the CWT and UHF conditions, respectively. The functional relationship between the Nusselt number, Prandtl number and the Reynolds number is seen to be qualitatively similar for both the thermal boundary conditions. It is seen that the average Nusselt number for the sphere increases with the increasing Reynolds number and/or Prandtl number. For the CWT condition, the present numerical data is best fitted by the correlation of Feng and Michaelides [14], Eq. (14). This equation correlates the present numerical data with the maximum and average deviations of 3.75% and 1.45%, respectively which are well within the limits of the stated uncertainty of this correlation. However, no prior analytical/numerical results are available for the UHF boundary condition. To fit the present numerical data for the UHF condition, the form of Eq. (14) is retained here along with the power indices, but with slightly different values of the constants as follows:

$$Nu = (1 + Pe^{1/3} + 0.158Re^{1/3}Pe^{1/3}) \tag{15}$$

Eq. (15) correlates the present numerical data with maximum and average deviations of 4.14% and 1.82%, respectively. The average Nusselt number is always higher for the UHF condition than that for the CWT condition, as is indicated by the constants in Eqs. (14) and (15). For in-

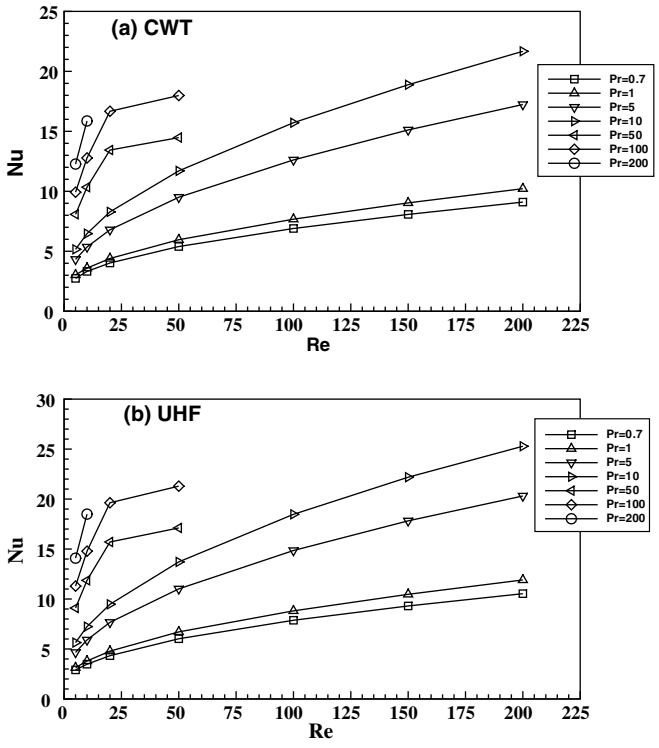

Fig. 6. Average Nusselt number as a function of Reynolds number at different Prandtl numbers: (a) CWT condition and (b) UHF condition.

stance, for $Re = 5$, and $Pr = 400$, the difference in the two values is of the order of 16%. This difference in the values of average Nusselt number increases with the Prandtl number and/or Reynolds number.

5. Conclusions

In the present study, the effects of Prandtl number ($0.7 \leqslant Pr \leqslant 400$) and of the two commonly used thermal boundary conditions on the forced convection heat transfer from an unconfined sphere have been investigated in the Reynolds number range of $5 \leqslant Re \leqslant 200$ in the steady symmetric regime. For $Re > 20$, the local Nusselt number on the sphere surface decreases from its maximum at the front stagnation point up to the point of separation and then again increases from the point of separation to the rear stagnation point. The average Nusselt number increases monotonically with Reynolds number and/or Prandtl number and it is always higher for the UHF boundary condition than that for the CWT condition. While the present results for the CWT condition are in good agreement with the previous results, no prior results are available for the UHF condition. Finally, Eqs. (14) and (15) capture well the dependence of Nusselt number on the Reynolds and Peclet numbers. In addition, the dependence of the mean Nusselt number on the Reynolds and Prandtl numbers has been linked to the distribution of the local Nusselt number on the surface of the sphere.

Acknowledgement

We gratefully acknowledge several constructive suggestions made by the two anonymous reviewers.

Appendix A. Boundary condition in the azimuthal direction

The free slip and axisymmetry boundary conditions have been applied in the z (azimuthal) direction. This means that the azimuthal velocity is set to zero and the azimuthal gradient of all other variables including the tangential velocities should vanish. The implementation of this is demonstrated with the help of Fig. 3 for the left face.

The normal and the tangential velocities are calculated for both the real (middle) and fictitious (side) cells using the discretized azimuthal angle ϕ_z per cell as

$$V_{y1}^n = -V_{y1}\sin(\phi_z/2) + V_{z1}\cos(\phi_z/2)$$
$$V_{y2}^n = -V_{y2}\sin(\phi_z/2) + V_{z2}\cos(\phi_z/2)$$
$$V_{y1}^t = V_{y1}\cos(\phi_z/2) + V_{z1}\sin(\phi_z/2)$$
$$V_{y2}^t = V_{y2}\cos(\phi_z/2) + V_{z2}\sin(\phi_z/2)$$

Using these velocities, the normal component of velocity and the normal gradient of the tangential velocities can be calculated. Setting these two quantities equal to zero, the boundary conditions for the velocities can be obtained as follows:

$$V_{y1} = V_{y2}\cos(\phi_z) + V_{z2}\sin(\phi_z)$$
$$V_{z1} = V_{y2}\sin(\phi_z) - V_{z2}\cos(\phi_z)$$

One can similarly obtain the boundary conditions for the right face. The homogeneous Neumann (zero gradient) boundary conditions for the other variables can be easily implemented by putting their values in the fictitious side cells equal to the computed values in the middle cell i.e.,

$$\frac{\partial V_x}{\partial z} = 0, \quad \frac{\partial p}{\partial z} = 0, \quad \frac{\partial T}{\partial z} = 0$$

References

[1] R. Clift, J.R. Grace, M.E. Weber, Bubbles, Drops and Particles, Academic Press, New York, 1978.
[2] A.D. Polyanin, A.M. Kutepov, A.V. Vyazmin, D.A. Kazenin, Hydrodynamics, Mass and Heat Transfer in Chemical Engineering, Taylor and Francis, London, 2002.
[3] M. Kaviany, Principles of Convective Heat Transfer, Springer-Verlag, New York, 1994.
[4] F. Kreith, The CRC Handbook of Thermal Engineering, The Mechanical Engineering Handbook Series, CRC Press/Springer, New York, 2000.
[5] S. Whitaker, Forced convection heat transfer correlations for flow in pipes, past flat plates, single cylinders, single spheres, and flow in packed beds and tube bundles, AIChE J. 18 (1972) 361–371.
[6] A. Acrivos, T.D. Taylor, Heat and mass transfer from single spheres in Stokes flow, Phys. Fluids 5 (1962) 387–394.
[7] P.N. Choudhoury, D.G. Drake, Unsteady heat transfer from a sphere in a low Reynolds number flow, Quart. J. Mech. Appl. Math. 24 (1971) 23–36.

[8] I. Proudman, J.R.A. Pearson, Expansions at small Reynolds numbers for the flow past a sphere and a circular cylinder, J. Fluid Mech. 2 (1956) 237–262.
[9] S.C.R. Dennis, J.D.A. Walker, J.D. Hudson, Heat transfer from a sphere at low Reynolds numbers, J. Fluid Mech. 60 (1973) 273–283.
[10] B. Abramzon, C. Elata, Heat transfer from single sphere in Stokes flow, Int. J. Heat Mass Transfer 27 (1984) 687–695.
[11] G.R. Ahmed, M.M. Yovanovich, Approximate analytical solution of forced convection heat transfer from isothermal spheres for all Prandtl numbers, Trans. ASME, J. Heat Transfer 116 (1994) 838–843.
[12] A.A. Kendoush, Low Prandtl number heat transfer to fluids flowing past an isothermal spherical particle, Int. J. Heat Fluid Flow 16 (1995) 291–297.
[13] Z.-G. Feng, E.E. Michaelides, Unsteady heat transfer from a spherical particle at finite Peclet numbers, J. Fluids Eng. 118 (1996) 96–102.
[14] Z.-G. Feng, E.E. Michaelides, A numerical study on the transient heat transfer from a sphere at high Reynolds and Peclet numbers, Int. J. Heat Mass Transfer 43 (2000) 219–229.
[15] E. Achenbach, Experiments on the flow past spheres at very high Reynolds numbers, J. Fluid Mech. 54 (1972) 565–575.
[16] E. Achenbach, Vortex shedding from spheres, J. Fluid Mech. 62 (1974) 209–221.
[17] V. Eswaran, S. Prakash, A finite volume method for Navier–Stokes equations, in: Proceedings of the Third Asian CFD Conference, Bangalore, India, 1998, pp. 127–136.
[18] A. Sharma, V. Eswaran, A finite volume method, in: K. Muralidhar, T. Sundararajan (Eds.), Computational Fluid Flow and Heat Transfer, Narosa Publishing House, New Delhi, 2003, pp. 445–482.
[19] I. Orlanski, A simple boundary condition for unbounded hyperbolic flows, J. Comp. Phys. 21 (1976) 251–269.
[20] J.F. Thompson, Z.U.A. Warsi, C.W. Mastin, Numerical Grid Generation: Foundation and Application, Elsevier North-Holland, Inc., New York, 1985.
[21] B.P. Leonard, A stable and accurate convective modeling procedure based on quadratic upstream interpolation, Comp. Meth. Appl. Mech. Eng. 19 (1979) 59–98.
[22] U. Ghia, K.N. Ghia, C.T. Shin, High resolution for incompressible flow using the Navier–Stokes equations and a multigrid method, J. Comput. Phys. 48 (1982) 387–411.
[23] A.K. Verma, V. Eswaran, A solution method of Navier–Stokes equations on non-staggered grids, Int. J. Numer. Methods Fluids 30 (1999) 279–308.
[24] T.A. Johnson, V.C. Patel, Flow past a sphere up to Reynolds number of 300, J. Fluid Mech. 378 (1999) 19–70.
[25] B.P. LeClair, Viscous flow in multiple systems at intermediate Reynolds numbers, PhD thesis, MacMaster University, Hamilton, ON, 1970.
[26] H. Schlichting, Boundary-Layer Theory, seventh ed., McGraw-Hill, New York, 1979.
[27] P.J. Roache, Verification and Validation in Computational Science and Engineering, Hermosa Publishers, Albuquerque, 1998.
[28] A. Tripathi, R.P. Chhabra, T. Sundararajan, Power-law fluid flow over spheroidal particles, Ind. Eng. Chem. Res. 33 (1994) 403–410.
[29] B. Fornberg, Steady viscous flow past a sphere at high Reynolds numbers, J. Fluid Mech. 190 (1988) 471–489.
[30] S.C.R. Dennis, J.D.A. Walker, Calculation of the steady flow past a sphere at low and moderate Reynolds numbers, J. Fluid Mech. 48 (1971) 771–789.
[31] S. Taneda, Experimental investigation of the wake behind a sphere at low Reynolds numbers, J. Phys. Soc. Jpn. 11 (1956) 1104–1108.